Tunable Layer Orientation and Morphology in Vapor-Liquid-Solid Growth of One-Dimensional GeS van der Waals Nanostructures

Eli Sutter[1,*] Jacob S. French,[2] and Peter Sutter[2]

[1]*Department of Mechanical and Materials Engineering, University of Nebraska-Lincoln, Lincoln, NE 68588 (USA)*

[2]*Department of Electrical and Computer Engineering, University of Nebraska-Lincoln, Lincoln, NE 68588 (USA)*

ABSTRACT

Vapor-liquid-solid (VLS) growth of layered crystals produces van der Waals nanowires, an emerging class of one-dimensional (1D) nanostructures. The crystal structure of van der Waals materials, covalently bonded within and weakly interacting between the layers, not only gives rise to highly anisotropic properties but also provides opportunities for controlling the layer orientation in VLS growth processes. Here, we show that such control can be realized via additives to the VLS catalyst, using 1D GeS van der Waals nanostructures as a model system. Au-catalyzed VLS growth from a pure GeS precursor invariably yields GeS nanowires with layering along the nanowire axis. Adding a small amount of SnS to the GeS vapor reproducibly switches the morphology to high quality ribbon-like GeS nanostructures with two different layer stacking geometries, 'angled ribbons' consisting of two misaligned halves with layer stacking parallel to the ribbon axis, and 'tilted-layer ribbons' in which a single set of GeS sheets is tilted away from the nanowire axis. TEM imaging and chemical analysis show that SnS is not incorporated in the growing ribbons but remains confined to the VLS drop where its likely role is to change the wetting of the GeS sheets by the catalyst drop, thus modifying the morphology and layer orientation. Cathodoluminescence measurements on individual GeS nanoribbons demonstrates small modifications of the emission between the two types of ribbons, while the overall optoelectronic properties remain those of GeS. Our results demonstrate opportunities for tailoring the morphology of 1D van der Waals nanostructures by modifications to the catalyst used in vapor-liquid-solid growth processes.

*Corresponding author: esutter@unl.edu

1. INTRODUCTION

Recently a particular class of semiconductor nanostructures has emerged – 1D nanowires of 2D van der Waals crystals, which combine the distinct structure of layered materials, *i.e.*, covalent bonding within the layers and weak van der Waals bonding between them, and 1D confinement achieved in nanowires. This is distinct from efforts of separating quasi-1D nanostructures by exfoliation from bulk materials made possible by the presence of anisotropy in the crystal structure of transition metal trichalcogenides such as TiS_3,[1-2] $TaSe_3$,[3-4] $ZrSe_3$,[5] NbS_3,[6] Sb_2Se_3,[7-8] $Ta_2Pd_3Se_8$,[9] as well as 1D nanostructures in which the van der Waals units represent true 1D chains (V_2Se_9,[10] Nb_2Se_9,[11] etc.). It is well established that nanowires of conventional 3D semiconductors grow with a preferred crystal orientation, *e.g.*, with the symmetry axis along the [111] direction for Si and Ge nanowires.[12] The highly anisotropic properties (within the layers *versus* across the van der Waals gaps)[13-14] of van der Waals crystals provide a strong incentive for developing synthesis protocols by which the layer orientation in nanowires can be controlled. To date two canonical cases have been demonstrated, namely longitudinal (layer stacking along wire axis) and transverse (wire axis aligned with the layers) van der Waals nanowires, although in principle it should be possible to realize arbitrary angles between the layer stacking and the nanowire axis. So far, vdW nanowires from a few layered materials (GeS,[15-16] GaS,[17] GaSe,[18] SnSe,[19-20] In_2Se_3,[21-23] Bi_2Se_3)[24] have been reported. The stacking orientation appears to be selected spontaneously during the growth, and prior work shows roughly equal numbers of longitudinal[15, 17, 19-20, 23-24] and transverse (ribbon-like)[7-8, 17-18, 21, 23-25] vdW nanowires. Attempts to control the orientation have been rare. In a recent study on GaS nanowires, we demonstrated that the

type of metal catalyst used in vapor-liquid-solid (VLS) growth can define the stacking orientation.[17] Ag nanoparticle catalysts produced both transverse and longitudinal single-crystalline nanowires with length exceeding tens of microns, while Au catalysts yielded exclusively transverse (ribbon-like) nanowires. The different morphologies obtained using the different catalysts were linked to different wetting properties of the catalyst drops on the open edges and basal plane of GaS. The observed structural diversity calls for an identification of the factors that govern the crystal orientation so it can be controlled during growth.

The majority of van der Waals nanowires have been created by combining the concepts of VLS nanowire growth[26-27] and van der Waals epitaxy[28-30] of many individual layers with nanoscale lateral footprint. Central to the VLS process is a liquid catalyst drop that transports source atoms/molecules from the vapor phase to the nanowire growth front, and thus defines the position and diameter of the growing nanowire.[31] Here we explore the effect of the catalyst drop on the stacking of layers in nanostructures of van der Waals crystals. We focus on GeS, a prominent layered group IV chalcogenide semiconductor with potential in electronic and optoelectronic applications[13, 32] for telecommunications, computing, as visible light photodetectors with high sensitivity and broad spectral response,[32-34] and as absorbers for solar energy conversion.[35] GeS nanowires have been demonstrated as efficient light emitters[15, 36] with tunable interlayer twist.[37-38] VLS synthesized GeS nanowires using Au catalysts invariably show longitudinal stacking. The modification of the Au VLS catalyst by incorporation of additional species could change key properties, such as the wetting of the basal plane and possibly open up novel regimes for achieving and controlling different layer stacking.

Here we demonstrate the formation of high quality ribbon-like GeS nanostructures with two different morphologies and layer stacking geometries by introducing Sn, supplied from the vapor phase as SnS during growth, in order to modify the properties of the Au-rich VLS catalyst. We use transmission electron microscopy (TEM) imaging after the growth to determine the structure of the nanoribbons and of the catalyst particles. Chemical analysis in TEM shows the composition to be pure GeS without detectable incorporation of Sn, *i.e.*, the added Sn acts only as a modifier for the VLS catalyst. Finally, we use cathodoluminescence in scanning transmission electron microscopy (STEM-CL) with spatial resolution below the diffraction limit to establish the optoelectronic properties of individual GeS nanoribbons.

2. RESULTS AND DISCUSSION

GeS nanostructures were grown in a two-zone tube furnace quartz reactor by simultaneous thermal evaporation of GeS and SnS powders using Ar-2% H_2 as a carrier gas (see Methods for details). The Si(100) substrates were covered by a thin Au film, which dewets at the growth temperature (265-300°C) to generate a polydisperse array of supported Au nanoparticles, which catalyze the growth of the nanostructures. Control samples, in which the Au catalyst was exposed to GeS vapor alone, were prepared in order to compare the 1D nanostructure morphologies obtained under identical conditions without and with the addition of SnS. The growth from a pure GeS precursor yields the typical GeS nanowires[15, 37-38] (Figure 1 (a)) as well as nanowires decorated with plates and flakes[16, 36] (Figure 1 (e)) prepared earlier under similar conditions. The GeS nanowires show the presence of axial screw dislocation and the characteristic Eshelby twist, which manifests itself by gradual changes in electron diffraction pattern as the (*a*,

b) planes rotate around the nanowire axis.[37] As expected, the nanowires are longitudinally stacked with the GeS *c*-axis parallel to the nanowire axis (Figure 1).

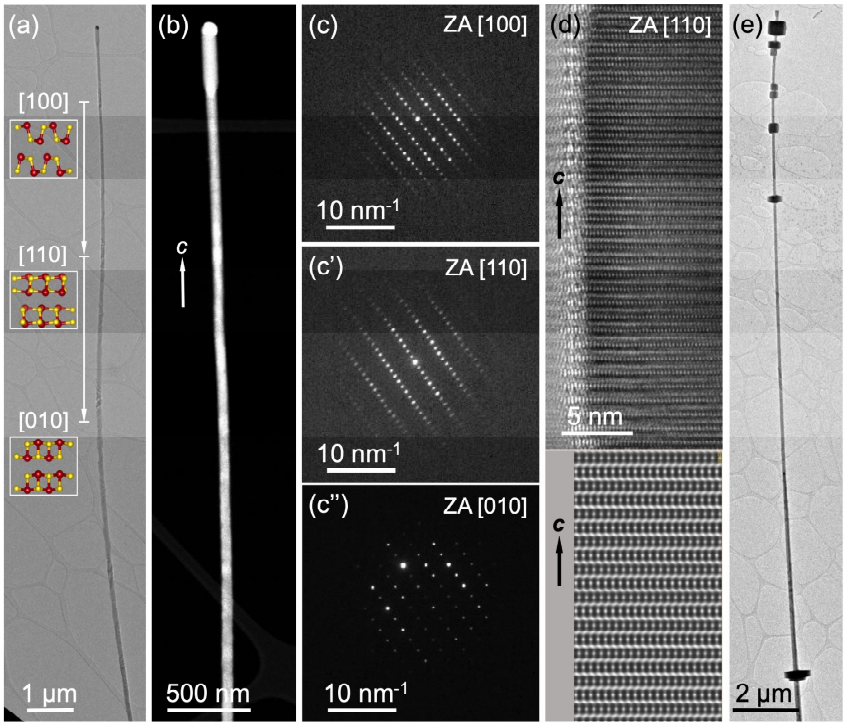

Figure 1. GeS nanowires by VLS growth over Au nanoparticle catalysts. (a), (b) TEM and HAADF-STEM images of a characteristic GeS nanowire grown on Si(100) substrate covered with nominally 2 nm Au film (substrate temperature: 300°C; precursor: GeS). The nanowire is longitudinally layered, *i.e.*, the GeS *c*-axis coincides with the nanowire axis. **(c)** Nanobeam electron diffraction patterns obtained at three positions labeled in (a). Eshelby twist due to an axial screw dislocation[37-38] causes a continuous rotation of the in-plane (*a*, *b*) crystal axes of the GeS wire so that the electron beam zone axis (ZA) gradually changes from [100] to [110] and finally [010]. **(d)** Top: High-resolution TEM image of the nanowire at a position corresponding to (c'), showing high quality crystalline GeS with stacking perpendicular to the nanowire axis. Bottom: GeS HRTEM image simulation along [110] zone axis. **(e)** GeS nanowire decorated with protruding GeS plates and flakes.

Adding SnS to the GeS vapor under otherwise identical conditions again yields forests of nanostructures (Figure 2 (a) and (b)), but induces drastic changes to the morphology. In addition, we find that the presence of SnS vapor widens significantly the temperature window (265°C–300°C) for the growth of GeS nanostructures, while the growth from pure GeS vapor occurs in a very narrow temperature range, (295 ± 5)°C. TEM of individual nanostructures transferred from the Si growth substrates to carbon

supports identifies the main morphologies as two different types of nanoribbons, angled and with tilted layers, respectively. The tilted-layer nanoribbons can be easily recognized in the TEM images (Figure 2 (c)) by a contrast similar to $Ge_{1-x}Sn_xS$ van der Waals ribbons,[39] notably with characteristic Kikuchi lines. The angled nanoribbons show a singular combination of dark and light contrast on the two edges (Figure 2 (d-d'')). Importantly, upon addition of SnS vapor, the characteristic twisted GeS nanowires obtained during growth from pure GeS powder (Figure 1) are no longer detected.

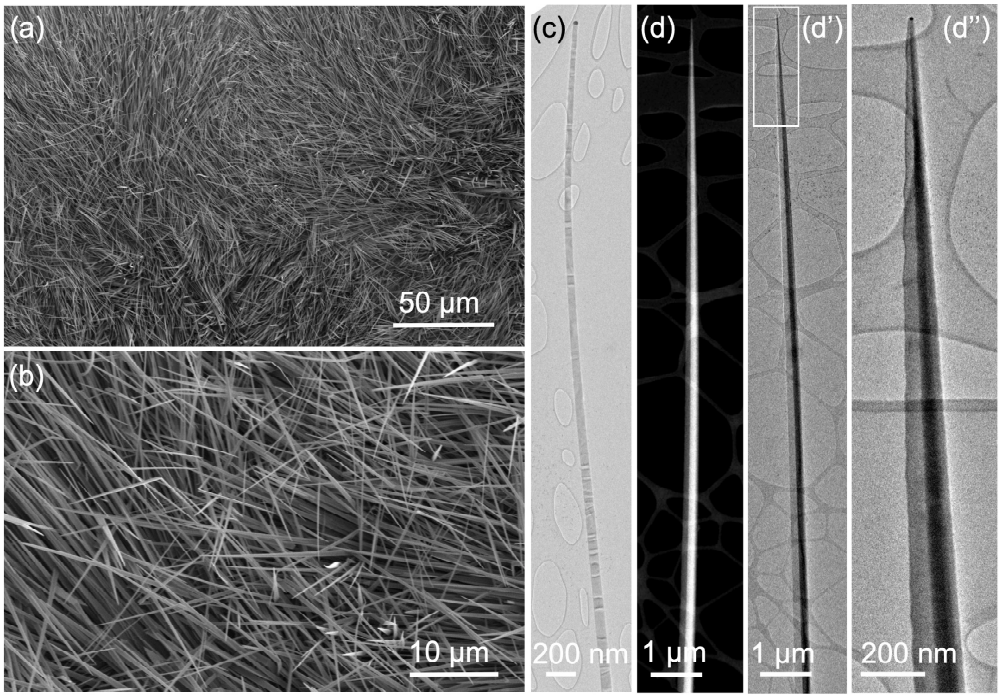

Figure 2. VLS growth of 1D nanostructures from GeS and SnS vapors. (a), (b) SEM images of GeS nanostructures grown on Si (100) substrate covered with nominally 2 nm Au film (substrate temperature: 300°C; precursor: GeS/SnS). **(c)** TEM image of a tilted-layer nanoribbon. **(d) – (d'')** HAADF-STEM and TEM images of angled nanoribbons.

We further investigated in detail the structure and composition of the two types of nanoribbons. Figures 3 and 4 summarize the results for the angled ribbons (see also Supplementary Figure S1). The TEM and the high-angle annular dark field (HAADF) STEM images (Figure 3 (a), (b)) of the angled nanoribbons show two well defined areas, in most cases with equal width but sometimes asymmetric, that show different contrast.

Generally, bright contrast in HAADF-STEM (Z-contrast imaging) stems either from a higher average atomic number (Z) or a larger thickness. As chemical imaging demonstrates, the areas with brighter and darker contrast have the same composition (see Figure 4 below), hence we conclude that the thickness of the two parts must be different to give rise to the different contrast. Electron diffraction (Figure 3 (c), (d)) identifies the crystal structure of both areas as single crystalline, orthorhombic layered GeS (space group Pnma).[13, 30] The area with light TEM contrast projects the GeS basal plane, *i.e.*, it is viewed along the [001] zone axis and bounded by (100) side facets; it represents a stack of GeS sheets arranged with their *c*-axis (the van der Waals stacking direction) perpendicular to the long axis of the nanoribbon. The same stacking orientation is observed in both layered $Ge_{1-x}Sn_xS$ nanoribbons[39] and gallium sulfide (GaS) nanoribbons synthesized with Ag and Au catalysts,[17] albeit in both cases uniformly over the entire ribbon width. High-resolution TEM in this part of the angled ribbons shows the lattice fringes characteristic of basal-plane oriented single crystalline few-layer GeS (Figure 3 (e)).

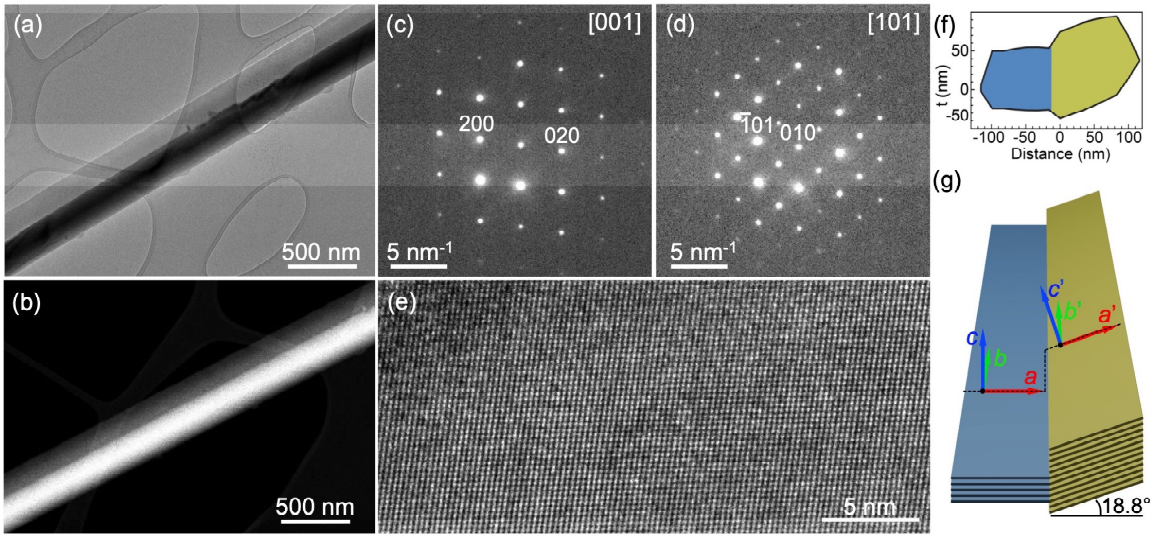

Figure 3. Morphology and structure of angled nanoribbons. (a), (b) TEM and HAADF-STEM images of a GeS nanoribbon grown on Si (100) substrate covered with nominally 2 nm Au film

(substrate temperature: 300°C; precursor: GeS/SnS). **(c), (d)** Nanobeam electron diffraction patterns of the parts of the angled nanoribbon showing light and dark contrast in TEM, respectively. **(e)** High-resolution TEM image of the lighter contrast area of the nanoribbon showing basal plane contrast of single crystalline GeS. **(f)** Thickness profile of an angled nanoribbon, derived from electron beam current attenuation measurements in HAADF-STEM, as described in Figures S1 and S2. **(g)** Schematic showing the geometry of the angled nanoribbons deduced from the TEM analysis. Note that other distributions of the thickness step at the central seam of the ribbon would also be consistent with our data (see Figure S2).

Electron diffraction patterns obtained in the parts with dark TEM contrast can be indexed to single crystalline GeS viewed along the [101] zone axis. The long axes of both parts of the nanoribbons are aligned along the [010] direction. This suggests that the nanostructure is an angled nanoribbon, whose two halves enclose an angle of 18.8°, as defined by the angle between the [101] and the [001] zone axes (Figure 3 (g)). The thickness profiles of the two parts were determined from electron beam current attenuation measurements calibrated using GeS nanowires with different diameters (Figure S1). The measurement of the thickness profile of a characteristic angled nanoribbon is shown in Figure S2 (b). This thickness profile is consistent with the finding of different thickness in the two parts of the nanoribbon and support different possible stitching configurations (with aligned or misaligned top and bottom layers) of the two parts as illustrated in Figure S2 (c) – (f). One of these configurations is also shown in Figure 3 (f).

In addition, nanobeam electron diffraction patterns were collected with a step of 15 nm across the ribbon (Figure S3). These linear arrays of diffraction patterns demonstrate that there is minimal overlap between the two portions of the angled ribbon. The transition between the ZA [001] diffraction pattern on the basal-plane oriented part of the nanoribbon to the ZA [101] pattern in the slanted part occurs within one 15 nm step. In Figure S3, there is only one spot at the central boundary that shows a superposition of both diffraction patterns. Since the geometric elongation due to the tilt cannot explain the

substantial contrast difference, we conclude that the darker contrast in TEM (bright contrast in STEM) is a consequence of a greater thickness of this part of the nanoribbon (Figure 3 (f)).

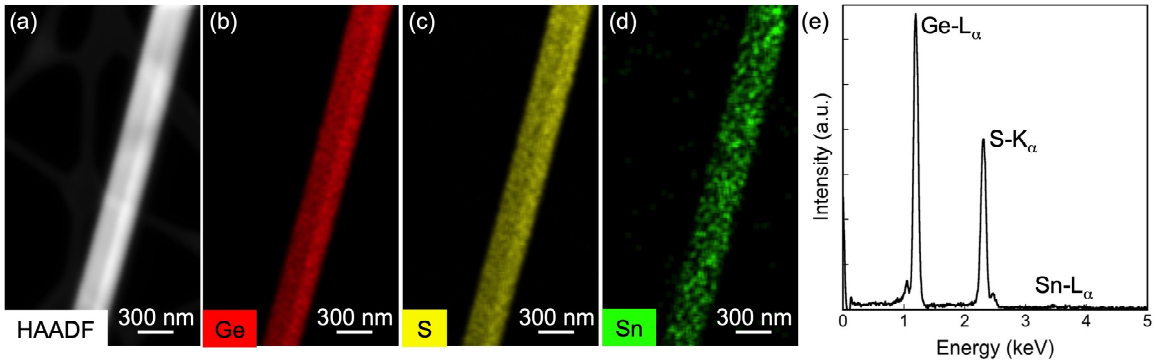

Figure 4. Chemical analysis of angled GeS nanoribbons. (a) HAADF-STEM image of a segment of a representative angled GeS nanoribbon. **(b)-(d)** EDS chemical maps of the nanoribbon showing the distribution of Ge (red), S (yellow), and Sn (green). **(e)** EDS spectrum from the nanoribbon.

Chemical analysis by energy-dispersive X-ray spectroscopy (EDS) in STEM detects Ge, S, as well as trace amounts of Sn in the angled van der Waals nanoribbons, *i.e.*, they consist of nearly pure GeS (Figure 4). The elemental maps also confirm that the two parts of the angled ribbon have different thickness, as the intensity of the Ge and S signals in the right half is higher, consistent with greater thickness. Importantly, EDS spectra of the nanoribbons shows very weak Sn intensity. Quantitative EDS analysis yields an average Sn content well below 1% under typical synthesis conditions at 300°C, despite the simultaneous exposure to GeS and SnS vapors during growth. Thus, the structural as well as the chemical characterizations confirm that the nanoribbons contain negligible amounts of Sn and consist of nearly pure GeS.

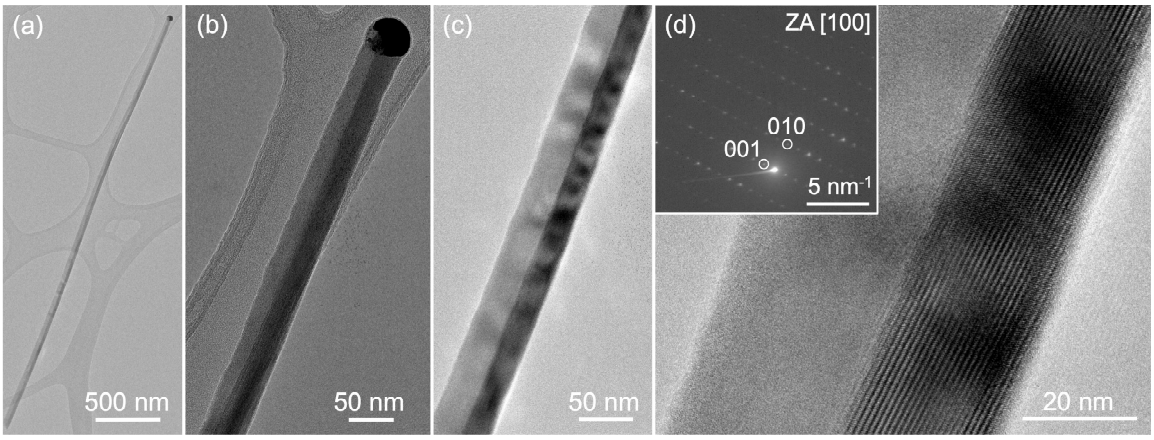

Figure 5. Van der Waals layering in angled nanoribbons. (a) TEM image of a GeS nanoribbon grown on Si (100) substrate covered with nominally 2 nm Au film (substrate temperature: 265°C; precursor: GeS/SnS). **(b), (c**) Higher magnification TEM images showing details of the angled ribbon near the Au particle at the tip. **(d)** High-resolution TEM image of the darker contrast portion of the nanoribbon showing the GeS van der Waals layering. Inset: Nanobeam electron diffraction patterns of the dark contrast part of the angled nanoribbon (zone axis (ZA): [100]).

Investigation of angled nanoribbons grown at different temperatures show that their sizes depend on the growth temperature. This allows us to grow angled nanoribbons with lateral sizes that can be varied in a wide range, from ~50 nm to ~200 nm. TEM images of a ribbon formed at 265°C (Figure 5) show that a lowering of the growth temperature causes the angled ribbons to become straighter, less tapered and significantly narrower than at higher temperatures (Figure 2 (d)). In the ribbon shown in Figure 5, the angled side is oriented close to the [100] zone axis so that the layering in this portion is seen edge-on, showing a thickness of ~20 GeS layers.

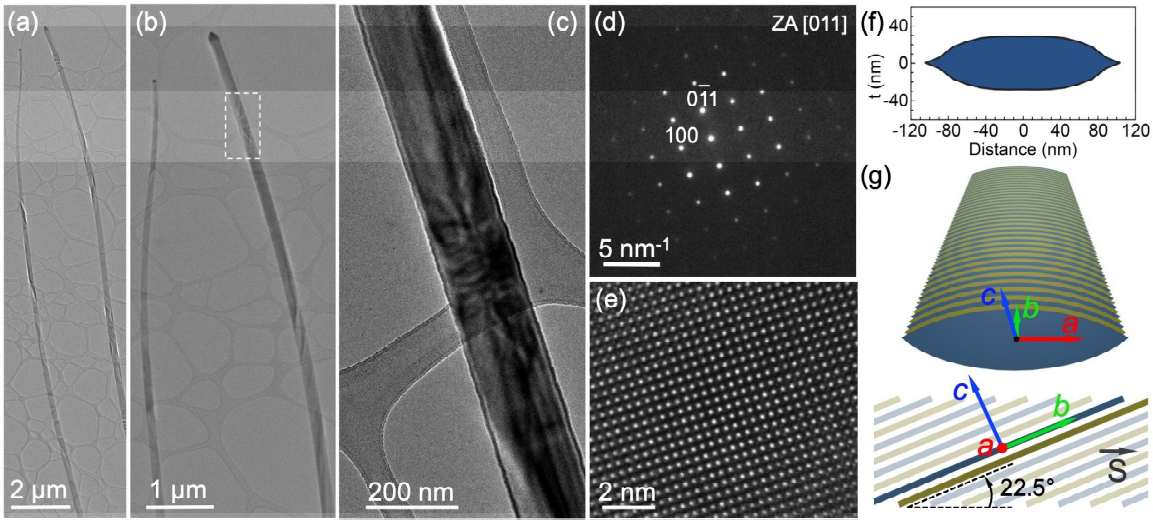

Figure 6. Morphology of tilted-layer nanoribbons. (a), (b) TEM images of two characteristic GeS nanoribbons grown on Si (100) substrate covered with nominally 2 nm Au film (substrate temperature: 275°C; precursor: GeS/SnS). **(c**) Higher magnification TEM image showing details of the ribbon in (b). **(d)** Selected-area electron diffraction pattern of the nanoribbon, showing its alignment along the [011] zone axis (ZA). **(e)** High-resolution TEM image of the nanoribbon. **(f)** Thickness profile of a tilted-layer nanoribbon, derived from electron beam current attenuation measurements in HAADF-STEM, as described in Figure S1 and S6. **(g)** Schematic of the structure of the tilted-layer nanoribbons. Top: Perspective view. Bottom: Side view. Note the tilting of the layers by an angle of 22.5° from the horizontal. S: symmetry axis of the nanoribbon.

The structure of the tilted-layer nanoribbons with different sizes is shown in Figure 6 and in Figures S4-S6. The nanoribbons appear straight and can have lengths of up to several tens of micrometers, while their lateral sizes vary in the range between 50 nm and 180 nm. Electron diffraction (Figure 6 (d), S5 (c)) confirms the single-crystallinity of the nanoribbons. For horizontally supported ribbons, the diffraction patterns are invariably viewed such that the electron beam projects along the [011] direction. This means that these nanostructures represent an intermediate case between the canonical longitudinal (layer stacking along wire axis) and transverse (wire axis aligned with the layers) van der Waals nanowires. In particular, the weakly coupled GeS van der Waals layers are not stacked along the symmetry axis as in traditional nanoribbons[39] and flakes[13] reported earlier, but the GeS sheets are tilted by 22.5° (Figure 6 (g)). High-resolution TEM images of the flat nanoribbons (Figure 6 (e)) show lattice fringes consistent with single-

crystalline, 22.5° off-axis layered GeS (imaged along the [011] zone axis).[40] We note that similar [011] oriented stacks (SnS sheets tilted by 21°) were observed under non-equilibrium conditions in kinetically driven processes, *e.g.*, the electron-beam driven transformation from SnS_2 to SnS.[41-42] Thickness profiles of the tilted-layer ribbons (Figure 6 (f) and Figure S6), were determined by measuring the attenuation of the beam current in HAADF-STEM, calibrated by measurements on nanowires (as shown in Figure S1). The measured beam current attenuation, which provides a thickness profile across different nanoribbons (along the lines shown in Figure S6 (a), (c), (e)), was translated into the shown profile by assuming a symmetric shape (Figure S6 (b), (d), (f)). The assumption of a symmetric shape is supported by direct HAADF-STEM imaging of a short broken-off section of a tilted-layer nanoribbon, shown in Figure S6 (g). The combined evidence from imaging, diffraction and beam attenuation thickness profile measurements allows us to conclude that the tilted layer nanoribbons morphology can be represented by the schematic shown in Figure 6 (g).

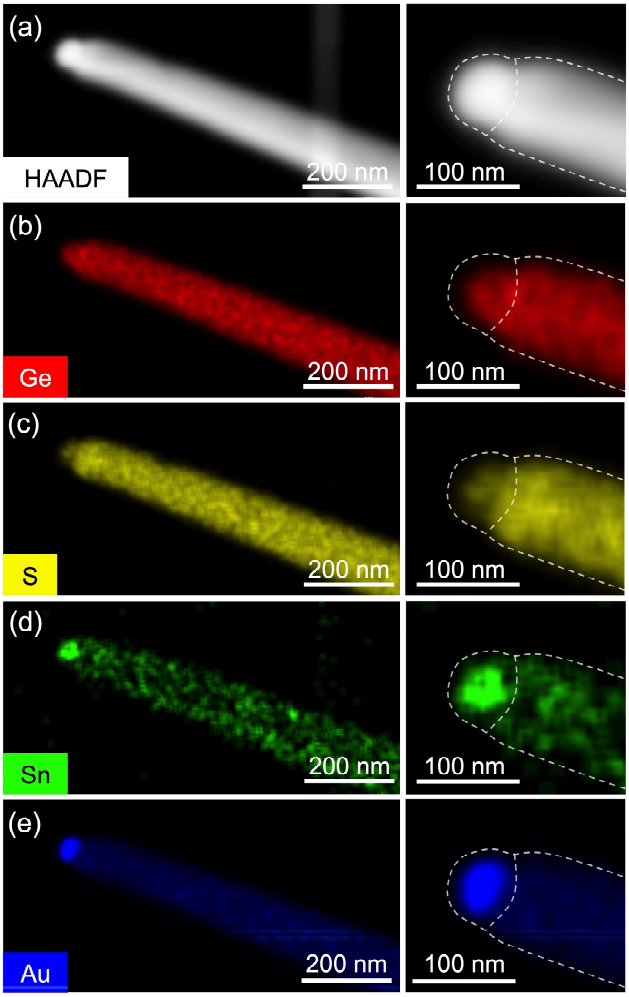

Figure 7. Chemical analysis of tilted-layer GeS nanoribbons (a) HAADF-STEM image of a representative tilted-layer GeS nanoribbon near the Au-rich tip. **(b) - (e)** EDS chemical maps of the GeS nanoribbon showing the distribution of Ge (red), S (yellow), Sn (green), and Au (blue). Panels on the right show a detailed view of the tip region, with dashed lines added as guides to the eye. Note that the Au signal is centered in the tip, whereas the Sn signal is offset from the center suggesting some phase separation during cooling from the growth temperature.

Figure 7 shows EDS elemental maps and spectra of a representative tilted-layer nanoribbon close to its tip (*i.e.*, the VLS catalyst). The maps demonstrate the uniform distribution of Ge and S within the ribbon (Figure 7 (b) – (c)). The EDS spectrum of the ribbon (Figure S7, black) shows Ge and S, but nearly undetectable Sn consistent with a low Sn signal shown in the EDS map (Figure 7 (d)). The Au EDS map shows apparent uniform Au signal across the entire ribbon (Figure 7 (e)), but we note that it actually

originates from the tail of the S-Kα peak (centered at 2.3 keV), which overlaps with the position of the Au-Mα peak (2.1 keV; Figure S7, red). Figure 7 also shows zoomed-in EDS maps detailing the composition near the VLS catalyst. This area contains Au, as well as Ge, S, and Sn. While Au is uniformly distributed in the tip, the Sn distribution is somewhat asymmetric to one side indicative of some degree of phase separation during cooling from the growth temperature. Such separation is also evident in TEM and STEM imaging near the VLS catalyst (Figure S4). While narrow tilted-layer nanoribbons show a single, roughly spherical Au-rich (*i.e.*, high Z) region at the tip (Figure S4 (a), (b)), wider ribbons carry this spherical particle along with an adjacent larger volume with different contrast (but still higher average Z than the ribbon itself), formed by phase separation of the catalyst drop during cooling (Figure S4 (c), (d)).

Summarizing the results of the analysis of structure, morphology, and chemical composition, we conclude that adding small amounts of SnS to the main GeS growth precursor under typical VLS synthesis conditions for GeS nanowires[15, 38, 43] over Au catalyst particles leads to formation of nanostructures with modified morphologies, *i.e.*, angled and tilted-layer nanoribbons while the composition remains pure GeS with barely detectable Sn content. We note that a low ratio between SnS and GeS vapor pressures (p(SnS):p(GeS) ~0.04, see Methods) is crucial to the use of SnS as a growth modifier without significant incorporation in the 1D nanostructures. Further increase of the SnS vapor pressure tends to lock in a basal-plane nanoribbon morphology and causes alloying. For instance, increasing the SnS vapor pressure (p(SnS):p(GeS) ~0.1) induces the formation of $Ge_{1-x}Sn_xS$ alloy nanoribbons (x ~ 0.1).[39] Au-rich catalyst particles are invariably found at the tips of both types of GeS nanoribbons, which suggests that their

growth proceeds *via* a VLS process,[15, 38, 44] in which molten alloy drops play the role of growth seeds and transport media whose interface to the semiconductor wire represents growth front of the 1D nanostructures. Whereas the VLS catalyst of GeS nanowires obtained with pure GeS precursor (Figure 1) contains only Au, Ge, and S,[15] EDS analysis clearly shows the presence of Sn in the tips of the nanoribbons obtained with SnS:GeS (Figure 7). This change to the VLS catalyst directly correlates with the observed modifications to the morphology of the layered nanostructures. Note that, on the other hand, the minimal incorporation of SnS (or Sn) in the nanoribbons (concentration below 1 at. %) is not expected to cause the changes in morphology observed here, given that SnS and GeS are isostructural and that the lattice constant of a SnS:GeS alloy with 0.1% SnS content deviates by less than 0.1% from that of pure GeS (lattice match along the b-direction; mismatch of 9.7% along the a-direction for the pure phases). Hence a nanostructure made of this alloy would essentially behave like pure GeS, which is also confirmed by our optoelectronic measurements (see below). This is also supported by recent findings that mixed/alloyed areas between GeS and SnS retain the crystal structure, morphology, and layering orientation of the corresponding host material independent of the Sn:Ge ratio, over the full composition range between pure SnS and GeS.[30] We therefore conclude that the incorporation of traces of Sn cannot explain the observed morphology changes, and that the most likely role of the added SnS is to change the interfacial energy (and thus wetting angle) between the GeS sheets and the catalyst drop.

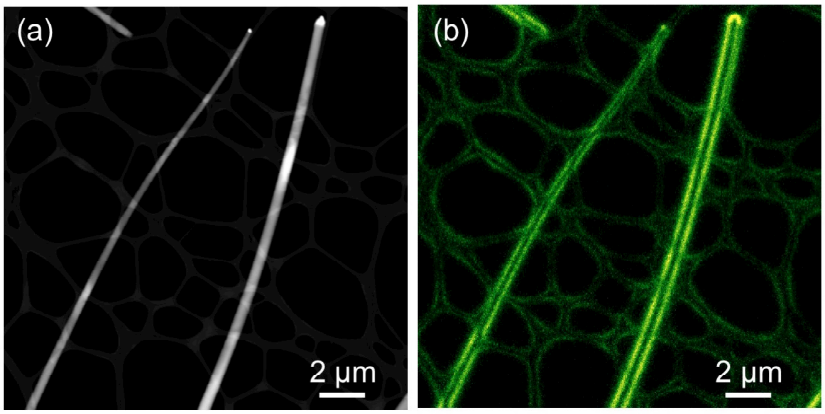

Figure 8. Panchromatic STEM-CL of GeS nanoribbons. (a) HAADF-STEM image of the tilted-layer nanoribbons shown in Figure 6. **(b)** Panchromatic CL map (wavelength range: 400-1000 nm) of the GeS nanoribbons shown in (a).

To evaluate the optoelectronic properties of the tilted GeS nanoribbons, we performed cathodoluminescence spectroscopy excited by the focused electron beam in STEM (STEM-CL). The high spatial resolution of STEM-CL enables the acquisition of luminescence spectra and hyperspectral linescans across individual nanoribbons. Figure 8 shows HAADF-STEM images and panchromatic CL maps of tilted-layer GeS nanoribbons dispersed on lacey carbon supports (see also Figure S8). The CL maps show bright luminescence with pronounced maximum in emission intensity observed near the edges of the ribbons.

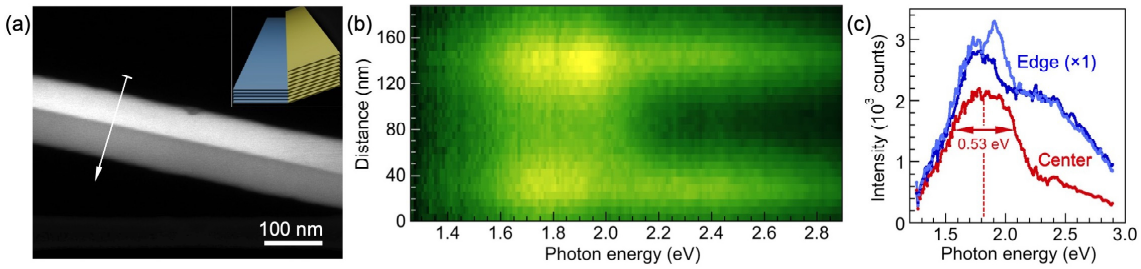

Figure 9. STEM-CL spectroscopy on individual angled GeS nanoribbons. (a) HAADF-STEM image of an angled nanoribbon, showing the characteristic sharp transition in image contrast. Inset: Schematic of the angled nanoribbon geometry. **(b)** Hyperspectral CL linescan (consisting of full spectra at each point) obtained along the line shown in (a). **(c)** Examples of individual CL spectra (part of the linescan in (b)), obtained at the center and the two edges of the nanoribbon.

Hyperspectral linescans, *i.e.*, sets of full CL spectra in linear arrays, were obtained across individual angled (Figure 9) and tilted-layer nanoribbons (Figure 10). The

linescans confirm the strong emission from the ribbon edges and the somewhat lower intensity of luminescence excited near the center (Figure 9 (b)). Individual CL spectra at the center of angled nanoribbons show a well-defined primary peak centered at ~1.82 eV (with full-width at half maximum (FWHM) 0.53 eV), whereas the edge spectra display additional intensity at higher photon energy (Figure 9 (c)), similar to GeS van der Waals nanowires.[15]

Figure 10 summarizes STEM-CL measurements on two tilted-layer nanoribbons with 22.5° off-axis stacked GeS sheets. Hyperspectral linescans (Figure 10 (c), (d)) and individual CL spectra (Figure 10 (e), (f)) are highly reproducible from ribbon to ribbon. The main emission peak detected in the center of the nanoribbons consistently lies just below 1.80 eV (FWHM ~ 0.4 eV) in different nanoribbons (Figure 10 (g)). This peak is

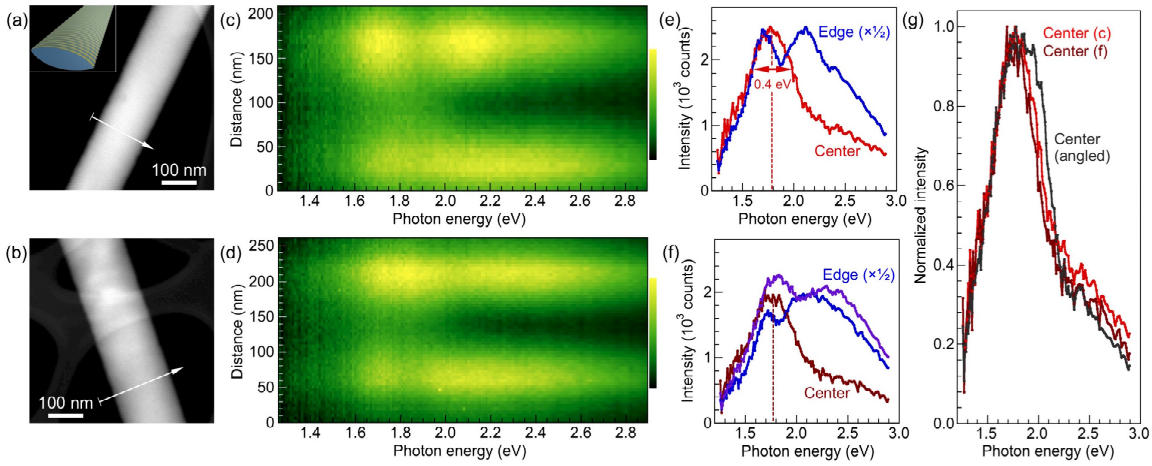

Figure 10. STEM-CL spectroscopy on individual tilted-layer GeS nanoribbons. (a), (b) HAADF-STEM images of two typical tilted layer GeS nanoribbons. Inset in (a): Schematic of the tilted-layer geometry. **(c), (d)** Hyperspectral linescans obtained along the lines shown in (a) and (b), respectively. **(e), (f)** Individual STEM-CL spectra obtained near the center and edge of the two tilted-layer nanoribbons. **(g)** Direct comparison of the luminescence spectra measured in the center of the two tilted-layer ribbons, and of the angled nanoribbon shown in Figure 9.

identical to luminescence peaks in GeS nanowires[15, 38, 43] as well as multilayer GeS flakes,[13] but its energy blue-shifts by different amounts relative to the bulk GeS bandgap

(~1.65 eV) due to quantum confinement.[13, 43] The GeS-like light emission provides additional evidence for the absence of significant incorporation of Sn in both angled and tilted-layer nanoribbons, since prior work has shown significant changes to the CL spectra even for $Ge_{1-x}Sn_xS$ alloys with low Sn content.[39] For electron beam excitation in the edge region, we find additional luminescence at higher photon energy (Figure 10 (e)) as well as broader peak centered at 2.40 eV that is invariably observed in GeS nanostructures.[13, 15, 39] The direct comparison between the two types of unconventional GeS ribbons discussed here shows consistently narrower band-edge luminescence (Figure 10 (g)) and significantly more intense edge emission (Figure 9 (c), Figure 10 (e)) for tilted-layer nanoribbons, reflecting the different electron beam excitation and light collection modes for the two types of nanostructures. Specifically, the electron-beam excitation and light emission from angled nanoribbons are similar to those in horizontal, basal-plane oriented ribbons, for which prior CL experiments and numerical simulations showed localized induced fields and broadband light emission.[39] In contrast, the tilted-layer nanoribbons project the GeS layers at a larger angle from the horizontal, which has been linked to more efficient electron beam excitation and narrower band-edge luminescence in STEM-CL.[39]

Finally, we note that wider nanoribbons show additional effects not found in their narrower counterparts. The sample shown in Figure S9, for example, shows very high luminescence intensity and pronounced modulations of the emitted intensity across the ribbon at discrete photon energies (Figure S9 (b)). In particular, at discrete energies of 1.65 eV and 1.85 eV we observe three and four intensity maxima, respectively (Figure S6 (c)). This intensity modulation is due to interference[36] of photonic modes excited by the

localized electron beam, propagating across the nanoribbons and reflected by specular surface facets (Figure S6 (d)), similar to recent observations in thick GaS nanowires.[17]

3. CONCLUSIONS

In summary, we establish that the addition of a modifier to the main growth precursor in vapor-liquid-solid growth of van der Waals crystals can be used to switch the accessible 1D morphologies by changing the wetting behavior of the VLS catalyst drop on the growing nanostructures. In the specific case studied here, adding SnS to the GeS vapor feeding the Au VLS catalyst changes the product from chiral twisted GeS nanowires with longitudinal van der Waals layering (*i.e.*, GeS *c*-axis parallel to the wire axis) to two types of nanoribbon architectures: Angled nanoribbons, in which a transverse layered GeS stack (GeS *c*-axis perpendicular to the symmetry axis) is joined to a second such stack at an angle of 18.8°; and tilted-layer nanoribbons, which are reminiscent of GeS nanowires but in which the individual layers are tilted to an angle of 22.5° from the central axis. The addition of the SnS modifier induces these morphology changes reproducibly under synthesis conditions that are otherwise identical to those used for the Au-catalyzed VLS growth of GeS nanowires, and without causing detectable alloying of Sn into the 1D GeS nanostructures. Cathodoluminescence measurements on individual 1D ribbons using nanometer-scale excitation by a focused electron beam show optoelectronic properties of the two types of van der Waals nanoribbons induced by SnS that are similar to those of GeS nanowires, but their spectra exhibit subtle differences due to the different orientation of the GeS layers within the different nanoribbons. Our results point to extensive opportunities for tailoring the morphology of 1D nanostructures of van der Waals crystals by modifications to the catalyst used in vapor-liquid-solid growth

processes. The tuning of the stacking orientation is likely enabled by large differences in surface energy between the basal plane and facets across layer edges, and the resulting preferential wetting of the liquid VLS catalyst drop. Further insight into the microscopic mechanisms underlying these changes could come from *in-situ* microscopy experiments during the synthesis of 1D van der Waals nanostructures, following protocols established previously for observing VLS growth of 3D crystalline nanowires.[45]

4. MATERIALS AND METHODS

GeS nanoribbons were synthesized using GeS powder (99.99%, Sigma Aldrich) and SnS powder (99.99%, Sigma Aldrich) precursors in a pumped quartz tube furnace with two independently controlled temperature zones. The GeS and SnS powders were placed in separate quartz crucibles and heated to 400-450°C and 620°C, respectively. These conditions result in vapor pressures of ~480 mTorr for GeS (450°C)[46] and ~20 mTorr for SnS (620°C).[46] For the preparation of control samples of GeS nanowires, only the crucible containing GeS was introduced in the system. The zone containing the substrates was heated to growth temperatures of 265-300°C. Pieces of Si(100) wafers covered with 2-4 nm thick Au films deposited by sputtering at room temperature were used as substrates. The ultrathin Au films dewet at the growth temperature, thus providing polydisperse Au nanoparticles as VLS growth catalysts. During growth, a Ar-2% H_2 carrier gas flow was maintained at 60 standard cubic centimeters per minute (sccm) and a pressure of 20 mTorr. Growth was typically performed for 10 minutes, resulting in the formation of nanoribbons with lengths of several tens of micrometers and thicknesses in the range 20 nm – 80 nm for the tilted-layer nanoribbons and down to ~20 nm (20 GeS

layers) for the angled nanoribbons. VLS growth performed in the range of temperatures between 265°C and 300°C yielded the same mixtures of tilted-layer and angled nanoribbons. For the TEM experiments thousands of nanowires were spread on carbon films (see Figure S10, which shows the characteristic density of the dispersed nanostructures). From the TEM samples we determine the ratio of tilted-layer to angled nanoribbons to be ~5:1. This might, however, result in undercounting of the number of the angled nanoribbons, probably related to the enhanced mechanical strength due to the layering parallel to the axis of this type of nanoribbon compared to the tilted-layer ribbons. We have surveyed ~100 tilted layer and angled nanoribbons using TEM imaging and electron diffraction and they invariably show the morphologies summarized in Figures 3 – 6, and S2-S6.

The morphology of the nanoribbons was investigated by transmission electron microscopy (TEM) and electron diffraction in an FEI Talos F200X; energy-dispersive X-ray spectroscopy (EDS) was carried out in an FEI Technai Osiris 80-200 ChemiSTEM field emission microscope. The optoelectronic properties were investigated by cathodoluminescence spectroscopy performed in STEM mode (STEM-CL) using a Gatan Vulcan CL holder at room temperature, 200 kV electron energy, and incident beam currents of 300-600 pA. Panchromatic CL maps (512×512 pixels, 1.28 ms per pixel) were acquired by scanning the exciting electron beam across the nanoribbons and recording the emitted light intensity across a broad wavelength range (400-1000 nm). Hyperspectral linescans were acquired by displacing the electron beam in predefined equal steps across individual nanostructures and acquiring full CL spectra (integration time: 10 s per spectrum) at each beam position. Individual CL spectra shown in the figures were

extracted from such linescan datasets.

5. ACKNOWLEDGEMENTS

This work was supported by the National Science Foundation, Division of Materials Research, Solid State and Materials Chemistry Program under Grant No. DMR-1904843.

The EDS measurements were performed in the Nebraska Nanoscale Facility: National Nanotechnology Coordinated Infrastructure and the Nebraska Center for Materials and Nanoscience, which are supported by the National Science Foundation under Award ECCS: 2025298, and the Nebraska Research Initiative.

Supporting Information. Supplementary Figures S1 – S10: Thickness profile measurements of angled and tilted-layer nanoribbons determined form electron beam attenuation measurements; TEM/STEM and diffraction on angled GeS nanoribbons, VLS catalysts; EDS of a tilted layer nanoribbon and of its VLS catalyst; Panchromatic STEM-CL on angled and tilted-layer GeS nanoribbons.

REFERENCES:

1. Lipatov, A.; Wilson, P. M.; Shekhirev, M.; Teeter, J. D.; Netusil, R.; Sinitskii, A. Few-Layered Titanium Trisulfide (Tis3) Field-Effect Transistors. *Nanoscale* **2015**, *7*, 12291-12296.
2. Island, J. O.; Biele, R.; Barawi, M.; Clamagirand, J. M.; Ares, J. R.; Sánchez, C.; van der Zant, H. S. J.; Ferrer, I. J.; D'Agosta, R.; Castellanos-Gomez, A. Titanium Trisulfide (Tis3): A 2d Semiconductor with Quasi-1d Optical and Electronic Properties. *Scientific Reports* **2016**, *6*, 22214.
3. Liu, G.; Rumyantsev, S.; Bloodgood, M. A.; Salguero, T. T.; Shur, M.; Balandin, A. A. Low-Frequency Electronic Noise in Quasi-1d Tase3 Van Der Waals Nanowires. *Nano Lett* **2017**, *17*, 377-383.
4. Empante, T. A.; Martinez, A.; Wurch, M.; Zhu, Y.; Geremew, A. K.; Yamaguchi, K.; Isarraraz, M.; Rumyantsev, S.; Reed, E. J.; Balandin, A. A.; Bartels, L. Low Resistivity and High Breakdown Current Density of 10 Nm Diameter Van Der Waals Tase3 Nanowires by Chemical Vapor Deposition. *Nano Lett* **2019**, *19*, 4355-4361.
5. Guo, J.; Tao, J.; Zhang, Z.; Fei, L.; Li, D.; Jadwiszczak, J.; Wang, X.; Guo, Y.; Liao, X.; Zhou, Y. Controllable Thermal Oxidation and Photoluminescence Enhancement in Quasi-1d Van Der Waals Zrs3 Flakes. *ACS Applied Electronic Materials* **2020**, *2*, 3756-3764.
6. Bloodgood, M. A.; Wei, P.; Aytan, E.; Bozhilov, K. N.; Balandin, A. A.; Salguero, T. T. Monoclinic Structures of Niobium Trisulfide. *APL Materials* **2018**, *6*, 026602.
7. Zhai, T.; Ye, M.; Li, L.; Fang, X.; Liao, M.; Li, Y.; Koide, Y.; Bando, Y.; Golberg, D. Single-Crystalline Sb2se3 Nanowires for High-Performance Field Emitters and Photodetectors. *Adv Mater* **2010**, *22*, 4530-4533.
8. Yang, R. B.; Bachmann, J.; Pippel, E.; Berger, A.; Woltersdorf, J.; Gösele, U.; Nielsch, K. Pulsed Vapor-Liquid-Solid Growth of Antimony Selenide and Antimony Sulfide Nanowires. *Adv Mater* **2009**, *21*, 3170-3174.
9. Zhang, Q.; Liu, C.; Liu, X.; Liu, J.; Cui, Z.; Zhang, Y.; Yang, L.; Zhao, Y.; Xu, T. T.; Chen, Y.; Wei, J.; Mao, Z.; Li, D. Thermal Transport in Quasi-1d Van Der Waals Crystal Ta2pd3se8 Nanowires: Size and Length Dependence. *Acs Nano* **2018**, *12*, 2634-2642.
10. Chae, S.; Siddiqa, A. J.; Kim, B. J.; Oh, S.; Choi, K. H.; Lee, K. H.; Kim, H. Y.; Yu, H. K.; Choi, J.-Y. Isolation of Inorganic Molecular Chains from Rod-Like Bulk V2se9 Crystal by Liquid Exfoliation. *Rsc Adv* **2018**, *8*, 35348-35352.
11. Lee, W.-G.; Chung, Y. K.; Lee, J.; Kim, B. J.; Chae, S.; Jeong, B. J.; Choi, J.-Y.; Huh, J. Edge Defect-Free Anisotropic Two-Dimensional Sheets with Nearly Direct Band Gaps from a True One-Dimensional Van Der Waals Nb2se9 Material. *ACS Omega* **2020**, *5*, 10800-10807.
12. Picraux, S. T.; Dayeh, S. A.; Manandhar, P.; Perea, D. E.; Choi, S. G. Silicon and Germanium Nanowires: Growth, Properties, and Integration. *JOM* **2010**, *62*, 35-43.
13. Sutter, E.; Zhang, B.; Sun, M.; Sutter, P. Few-Layer to Multilayer Germanium(Ii) Sulfide: Synthesis, Structure, Stability, and Optoelectronics. *Acs Nano* **2019**, *13*, 9352-9362.
14. Sutter, P.; Wang, J.; Sutter, E. Wrap-around Core–Shell Heterostructures of Layered Crystals. *Adv Mater* **2019**, *31*, 1902166.

15. Sutter, E.; Sutter, P. 1d Wires of 2d Layered Materials: Germanium Sulfide Nanowires as Efficient Light Emitters. *ACS Applied Nano Materials* **2018**, *1*, 1042-1049.
16. Li, C.; Yu, Y.; Chi, M.; Cao, L. Epitaxial Nanosheet–Nanowire Heterostructures. *Nano Lett* **2013**, *13*, 948-953.
17. Sutter, E.; French, J. S.; Sutter, S.; Idrobo, J. C.; Sutter, P. Vapor–Liquid–Solid Growth and Optoelectronics of Gallium Sulfide Van Der Waals Nanowires. *Acs Nano* **2020**, *14*, 6117-6126.
18. Peng, H.; Meister, S.; Chan, C. K.; Zhang, X. F.; Cui, Y. Morphology Control of Layer-Structured Gallium Selenide Nanowires. *Nano Letters* **2007**, *7*, 199-203.
19. Liu, S.; Guo, X.; Li, M.; Zhang, W.-H.; Liu, X.; Li, C. Solution-Phase Synthesis and Characterization of Single-Crystalline Snse Nanowires. *Angewandte Chemie International Edition* **2011**, *50*, 12050-12053.
20. Butt, F. K.; Mirza, M.; Cao, C.; Idrees, F.; Tahir, M.; Safdar, M.; Ali, Z.; Tanveer, M.; Aslam, I. Synthesis of Mid-Infrared Snse Nanowires and Their Optoelectronic Properties. *CrystEngComm* **2014**, *16*, 3470-3473.
21. Zhai, T.; Fang, X.; Liao, M.; Xu, X.; Li, L.; Liu, B.; Koide, Y.; Ma, Y.; Yao, J.; Bando, Y.; Golberg, D. Fabrication of High-Quality In2se3 Nanowire Arrays toward High-Performance Visible-Light Photodetectors. *Acs Nano* **2010**, *4*, 1596-1602.
22. Hsu, Y.-C.; Hung, Y.-C.; Wang, C.-Y. Controlling Growth High Uniformity Indium Selenide (In2se3) Nanowires Via the Rapid Thermal Annealing Process at Low Temperature. *Nanoscale Res. Lett.* **2017**, *12*, 532.
23. Peng, H.; Xie, C.; Schoen, D. T.; Cui, Y. Large Anisotropy of Electrical Properties in Layer-Structured In2se3 Nanowires. *Nano Lett* **2008**, *8*, 1511-1516.
24. Zou, Y.; Chen, Z.-G.; Huang, Y.; Yang, L.; Drennan, J.; Zou, J. Anisotropic Electrical Properties from Vapor–Solid–Solid Grown Bi2se3 Nanoribbons and Nanowires. *The Journal of Physical Chemistry C* **2014**, *118*, 20620-20626.
25. Alegria, L. D.; Yao, N.; Petta, J. R. Mocvd Synthesis of Compositionally Tuned Topological Insulator Nanowires. *physica status solidi (RRL) – Rapid Research Letters* **2014**, *8*, 991-996.
26. Wagner, R. S.; Ellis, W. C. Vapor-Liquid-Solid Mechanism of Single Crystal Growth. *Applied Physics Letters* **1964**, *4*, 89-90.
27. Givargizov, E. I. Fundamental Aspects of Vls Growth. *Journal of Crystal Growth* **1975**, *31*, 20-30.
28. Koma, A.; Sunouchi, K.; Miyajima, T. Fabrication and Characterization of Heterostructures with Subnanometer Thickness. *Microelectronic Engineering* **1984**, *2*, 129-136.
29. Koma, A.; Sunouchi, K.; Miyajima, T. Summary Abstract: Fabrication of Ultrathin Heterostructures with Van Der Waals Epitaxy. *Journal of Vacuum Science & Technology B: Microelectronics Processing and Phenomena* **1985**, *3*, 724-724.
30. Sutter, E.; Wang, J.; Sutter, P. Lateral Heterostructures of Multilayer Ges and Sns Van Der Waals Crystals. *Acs Nano* **2020**, *14*, 12248-12255.
31. Sutter, E. A.; Sutter, P. W. Size-Dependent Phase Diagram of Nanoscale Alloy Drops Used in Vapor−Liquid−Solid Growth of Semiconductor Nanowires. *ACS Nano* **2010**, *4*, 4943-4947.

32. Ulaganathan, R. K.; Lu, Y.-Y.; Kuo, C.-J.; Tamalampudi, S. R.; Sankar, R.; Boopathi, K. M.; Anand, A.; Yadav, K.; Mathew, R. J.; Liu, C.-R.; Chou, F. C.; Chen, Y.-T. High Photosensitivity and Broad Spectral Response of Multi-Layered Germanium Sulfide Transistors. *Nanoscale* **2016**, *8*, 2284-2292.
33. Lan, C.; Li, C.; Yin, Y.; Guo, H.; Wang, S. Synthesis of Single-Crystalline Ges Nanoribbons for High Sensitivity Visible-Light Photodetectors. *Journal of Materials Chemistry C* **2015**, *3*, 8074-8079.
34. Dhanabalan, S. C.; Ponraj, J. S.; Zhang, H.; Bao, Q. L. Present Perspectives of Broadband Photodetectors Based on Nanobelts, Nanoribbons, Nanosheets and the Emerging 2d Materials. *Nanoscale* **2016**, *8*, 6410-6434.
35. Antunez, P. D.; Buckley, J. J.; Brutchey, R. L. Tin and Germanium Monochalcogenide Iv-Vi Semiconductor Nanocrystals for Use in Solar Cells. *Nanoscale* **2011**, *3*, 2399-2411.
36. Sutter, P.; Argyropoulos, C.; Sutter, E. Germanium Sulfide Nano-Optics Probed by Stem-Cathodoluminescence Spectroscopy. *Nano Lett* **2018**, *18*, 4576-4583.
37. Sutter, P.; Wimer, S.; Sutter, E. Chiral Twisted Van Der Waals Nanowires. *Nature* **2019**, *570*, 354–357.
38. Sutter, P.; Idrobo, J.-C.; Sutter, E. Van Der Waals Nanowires with Continuously Variable Interlayer Twist and Twist Homojunctions. *Advanced Functional Materials* **2021**, *31*, 2006412.
39. Sutter, P.; Khorashad, L. K.; Argyropoulos, C.; Sutter, E. Cathodoluminescence of Ultrathin Twisted Ge1–Xsnxs Van Der Waals Nanoribbon Waveguides. *Adv Mater* **2021**, *33*, 2006649.
40. Wiedemeier, H.; Schnering, H. G. V. Refinement of the Structures of Ges, Gese, Sns and Snse. *Z Kristallogr* **1978**, *148*, 295-303.
41. Sutter, E.; Huang, Y.; Komsa, H. P.; Ghorbani-Asl, M.; Krasheninnikov, A. V.; Sutter, P. Electron-Beam Induced Transformations of Layered Tin Dichalcogenides. *Nano Lett* **2016**, *16*, 4410-4416.
42. Sutter, P.; Komsa, H.-P.; Krasheninnikov, A. V.; Huang, Y.; Sutter, E. Luminescence of Defects in the Structural Transformation of Layered Tin Dichalcogenides. *Applied Physics Letters* **2017**, *111*, 262102.
43. Sutter, P.; Wimer, S.; Sutter, E. Chiral Twisted Van Der Waals Nanowires. *Nature* **2019**, *570*, 354-357.
44. Li, C.; Yu, Y. F.; Chi, M. F.; Cao, L. Y. Epitaxial Nanosheet-Nanowire Heterostructures. *Nano Letters* **2013**, *13*, 948-953.
45. Ross, F. M. Controlling Nanowire Structures through Real Time Growth Studies. *Reports on Progress in Physics* **2010**, *73*, 114501.
46. Mills, K. C., *Thermodynamic Data for Inorganic Sulphides, Selenides and Tellurides*. Butterworths: London, 1974; p 328-332.

ToC Graphic